ACS Photonics

Article

pubs.acs.org/journal/apchd5

Ultracompact Position-Controlled InP Nanopillar LEDs on Silicon with Bright Electroluminescence at Telecommunication Wavelengths

Saniya Deshpande,[†] Indrasen Bhattacharya,[†] Gilliard Malheiros-Silveira, Kar Wei Ng, Fabian Schuster, Willi Mantei, Kevin Cook, and Connie Chang-Hasnain*

Department of Electrical Engineering and Computer Sciences, University of California at Berkeley, Berkeley, California 94720, United States

Supporting Information

ABSTRACT: Highly compact III−V compound semiconductor active nano-photonic devices integrated with silicon are important for future low power optical interconnects. One approach toward realizing heterogeneous integration and miniaturization of photonic devices is through nanowires/nanopillars grown directly on silicon substrates. However, to realize their full potential, the integration of nanowires/nanopillars with silicon-based electronics must be made scalable via precise control of nanopillar site and dimensions. Here we demonstrate the first electrical-pumped InGaAs/InP multiquantum-well (MQW) light emitting diodes (LED) using nanopillar array directly grown on a Si substrate with site control, with current conduction directly through the silicon. The growth is via catalyst-free, low-temperature metal organic chemical vapor deposition, which is CMOS compatible. We report excellent optical properties including long minority carrier lifetimes and room-temperature lasing under optical pumping. InGaAs/InP quantum wells are incorporated in the nanopillars in a core−shell growth mode, to obtain silicon transparent emission of ∼1510 nm with high internal quantum efficiency (∼30%). Despite its small footprint, a high output power (4 μW) was measured, and the device could be electrically biased to produce optical gain. CMOS-compatible site-controlled growth and electrically driven long-wavelength emission make the InP nano-LED an ideal component in advanced photonic integrated circuits.

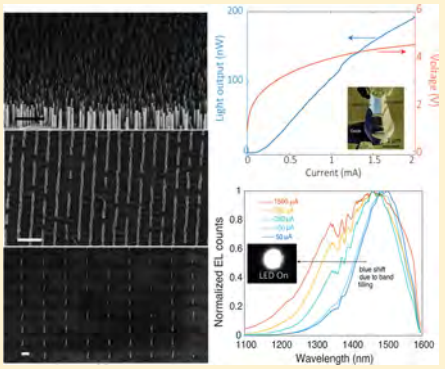

KEYWORDS: *nanowire/nanopillar, nanowire laser, LEDs, MOCVD growth, quantum-well, InP, III−V, photonic integrated circuit, silicon photonics*

With the ever-increasing demand for data-speeds and complexity in computing systems, interconnect density, throughput management and increasing bandwidth demand are becoming crucial challenges.[1] Optical interconnects are a potential solution to meet these challenges, and achieve performance requirements of current and future generations of data processors.[2−4] Since silicon itself is a poor choice for active photonic devices due to its indirect bandgap, there has been intense research toward developing low cost, high performance and Si-CMOS compatible optical components. III−V direct bandgap semiconductors demonstrate excellent optical properties and quantum efficiencies, surpassing silicon in all aspects but the cost.[5] Thus, the most promising strategy is to integrate high-performance III−V optical devices, such as emitters and detectors, on economic and ubiquitous silicon substrates.[6−10] However, heteroepitaxy of III−V on Si presents a major challenge due to the large lattice constant and thermal expansion mismatches. The particularly large 8% lattice mismatch between InP and Si, leads to high dislocation density of the order $\sim 10^8/cm^2$ in the grown layer resulting in poor luminescence efficiency.[11,12] III−V nanostructures, such as nanowires or nanopillars, circumvent this problem by allowing defects to terminate close to the interface and strain to relax radially.[13−15] Several groups have successfully demonstrated III−V nanowires on silicon substrates for various applications via different methods.[16−32]

Our group has previously reported InGaAs and InP nanoneedle or nanopillar structures on silicon substrates, grown at low-temperature (400−450 °C) by metal organic chemical vapor deposition (MOCVD).[18−23] The growth condition was verified to be back-end-of-line CMOS compatible.[24] The core−shell growth mode allows scaling up the diameters beyond lattice-mismatched critical dimensions, while still maintaining single crystallinity.[21] Due to their micron-scale dimensions, these structures do not suffer from the debilitating effects of surface recombination commonly seen in nanowires. InP nanopillars, in particular, exhibit a very low surface recombination velocity of 1.1×10^3 cm/s, which is comparable to InP bulk.[33]

Due to these unique properties, InP nanopillars have shown remarkable material and device performance in the form of optically pumped lasers,[18,19] photodetectors,[34] and solar cells.[35] However, for truly seamless and scalable integration of InP

Received: January 21, 2017
Published: February 21, 2017

DOI: 10.1021/acsphotonics.7b00065
ACS Photonics 2017, 4, 695−702

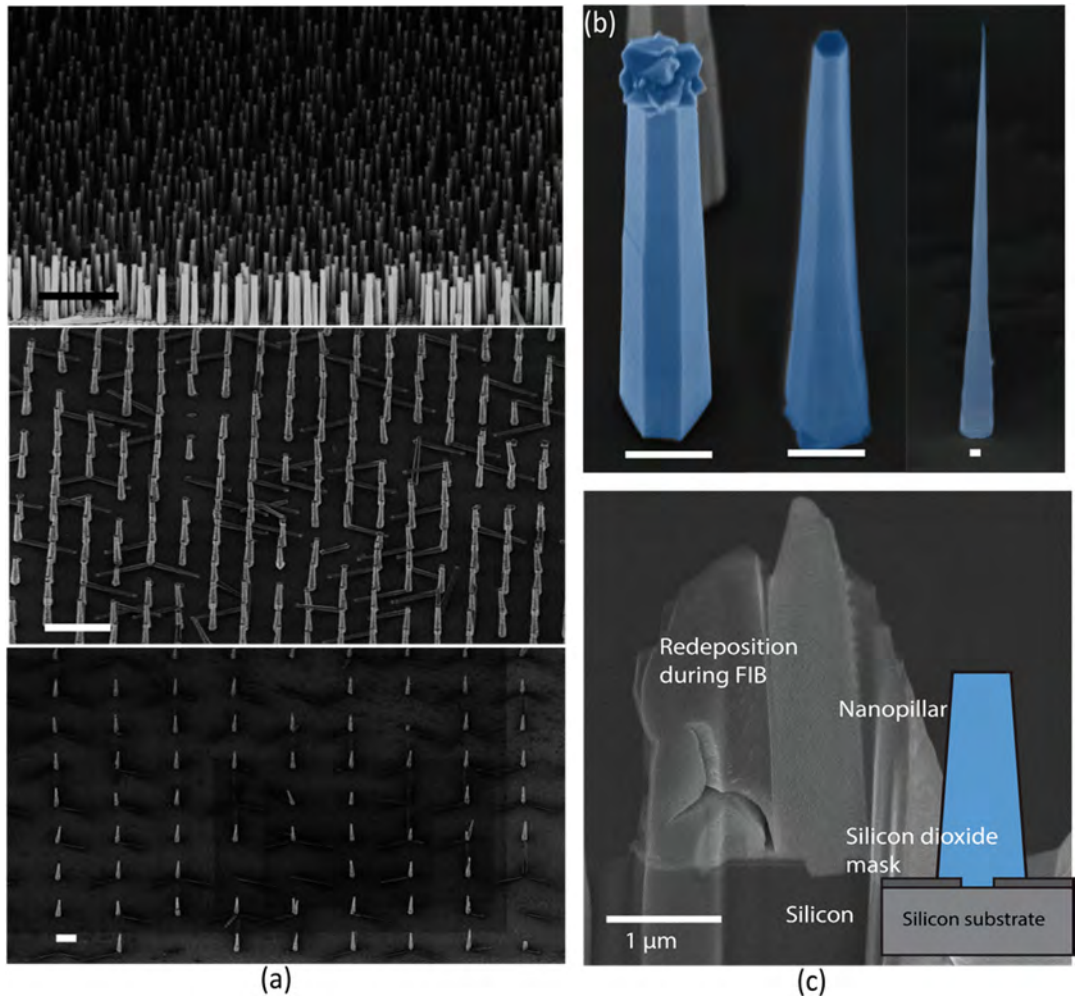

Figure 1. (a) Tilt-view low magnification SEM images of arrays of site-controlled InP nanopillars grown at 460 °C. The scale bar in all images corresponds to 10 μm and the growth periods (pitch) are 1 μm, 4 and 40 μm, respectively. (b) Nanopillars grown under the same nominal V/III ratio, for 15 min at 460, 455, and 450 °C, exhibit drastically different taper angles. The scale bar in all figures is 1 μm. (c) HAADF-STEM image of a cross-section of an InP nanopillar nucleating on Si, with a schematic representation in the inset.

photonic devices on silicon, it is imperative to grow InP nanopillars at predetermined locations. Additionally, randomly nucleated nanopillars suffer from variation in their morphology and structural properties, which ultimately affects uniformity of device characteristics. Position controlled growth will allow for a systematic study of the properties of the nanopillars. Previous reports of selective area growth on silicon have relied on gold nanoparticle catalysts or high growth temperature (usually >550 °C),[32,38] both of which have compatibility issues with CMOS back-end process requirements. There have also been several reports of site-controlled epitaxy of InP nanostructures on expensive native InP substrates.[36,37]

Here, we report the first site-controlled growth of high-yield, uniform arrays of InP nanopillars on silicon, grown under CMOS compatible conditions: low temperature and without catalysts. The structural properties such as taper and diameter are functions of MOCVD growth conditions. Excellent optical properties were verified through microphotoluminescence and time-resolved photoluminescence measurements. To achieve silicon transparent emission from the nanopillars, InGaAs/InP quantum wells were grown in the core−shell mode. In addition to growth parameters, photoluminescence from the InGaAs multiquantum wells is also a function of the nanopillar period/pitch, which adds another degree of freedom to control emission wavelength. The InGaAs/InP quantum wells in the nanopillars were investigated through temperature and pump dependent photoluminescence, which reveals bright, efficient and sharp emission. Finally, nanopillar-based multiquantum well LEDs were successfully grown and fabricated using an all optical-lithography process, with electrical conduction directly through the silicon substrate. Nanopillar LEDs exhibit radiative dominant electroluminescence around 1500 nm with high output power (4 μW), despite their small footprint.

CMOS COMPATIBLE SITE-CONTROLLED GROWTH OF NANOPILLARS

Position-controlled growth of InP nanopillars on (111) silicon is achieved using a silicon dioxide growth mask. Approximately, 140 nm of silicon dioxide is deposited on a clean silicon wafer by low temperature (350 °C), plasma-enhanced chemical vapor deposition (PECVD). Nanoscale apertures (~320 nm diameter) are defined in the oxide using DUV lithography, and reactive ion etching is used to etch the oxide and access the Si substrate. The growth mask contains apertures with the pitch varying from 1 to 40 μm. Prior to loading the substrate in the Emcore D75 MOCVD reactor, the silicon surface is chemically

DOI: 10.1021/acsphotonics.7b00065
ACS Photonics 2017, 4, 695−702

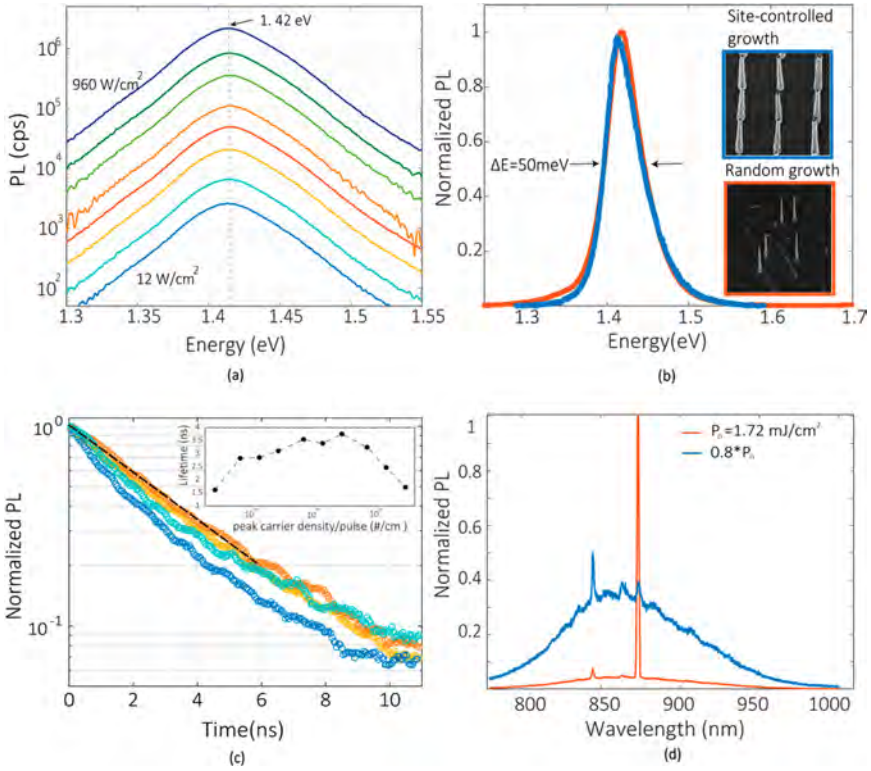

Figure 2. (a) Room-temperature photoluminescence measured from a single nanopillar grown at 460°, as a function of excitation powers, shows a single wurtzite peak at 1.42 eV. (b) Emission from a site-controlled nanopillar and spontaneously nucleated nanopillars shows comparable line widths. Inset shows SEM images of both samples. (c) Time-resolved PL spectra measured from a nanopillar for different pump powers. An intrinsic InP nanopillar shows a lifetime v/s carrier density trend as shown in the inset, with a peak lifetime of 3.7 ns. (d) Spectra from a single n-InP nanopillar below and above lasing threshold at room temperature.

roughened using tetramethylammonium hydroxide (TMAH) and deoxidized using dilute-buffered hydrofluoric acid (BHF), which were found to be crucial for nanopillar nucleation on silicon. In the MOCVD chamber, the substrate is first heated in TBP ambient before initiation of growth. Growth of InP nanostructures studied here was carried out between 450 and 460 °C for 15 min, after an initial 3 min annealing step at 550 °C. Under optimized growth conditions, nanopillar growth is performed under nominal TBP partial pressure of 56.3 mTorr and TMIn partial pressure of 0.55 mTorr. This results in highly regular arrays of InP nanopillars for various growth pitch sizes (1, 4, and 40 μm), as shown in the large-scale tilt-view scanning electron microscopy (SEM) image in Figure 1a. Site-controlled growth leads to increased uniformity of nanopillar dimensions, with a standard deviation in diameter of <10%. Due to the relatively large size of the oxide apertures, in addition to upright pillars, some growth apertures have slanted micropillars nucleating along the equivalent ⟨111⟩ directions of silicon. High growth yield exceeding 90% is obtained for all array periods. The pillars show some variation of taper angle in different arrays due to differences in local group III/V ratio. As seen in Figure 1b, the morphology and structure of nanopillars can be engineered considerably by tweaking growth conditions. Under the same TMIn and TBP flow rates, nanoneedles are observed at a growth temperature of 450 °C. The taper angle decreases as temperature is increased to 455 °C. Nearly vertical pillar-shaped structures are obtained at 460 °C. Further increase in temperature, under a constant TMIn flow rate, adversely affects the nanopillar nucleation density. With increase in substrate temperature, the cracking efficiency of TBP increases, which results in higher TBP partial pressure. Similar to the findings of Fukui et al. in InP nanowires grown on native InP (001) substrates, we observe an increase in lateral growth with higher TBP partial pressure.[36] Under high TBP partial pressure, this may be attributed to the adsorption and bonding of P atoms to In atoms along the ⟨110⟩ direction, providing additional dangling bonds for the attachment of the In species, thereby enhancing the lateral growth rate. From our previous investigation on InGaAs nanopillars, we have found that the taper angle of nanopillars has an effect on the nature of the cavity and its quality factor.[20,39] To investigate nanopillar nucleation and growth on silicon, we studied its cross-section using transmission electron microscopy. Using a micromanipulator and focused ion beam (FIB), a thin slice or lamella of the heterointerface was prepared. The top part of the InP pillar was removed using the focused ion beam, and Pt was then deposited onto the gap to passivate the heterointerface during the subsequent ion beam milling process. Figure 1c shows a cross-sectional high-angle annular dark field scanning transmission electron microscope (HAADF-STEM) image of the nanopillar nucleating directly on the silicon opening in the oxide. Due to its core−shell growth mode, the nanopillar finally grows out of the oxide opening and assumes a final diameter of ∼1 μm. We previously found that periodic misfit dislocations effectively relax the misfit stress between Si/InP, leading to the high-quality, defect-free growth in the bulk material of the InP pillar away from the heterointerface.[33]

DOI: 10.1021/acsphotonics.7b00065
ACS Photonics 2017, 4, 695−702

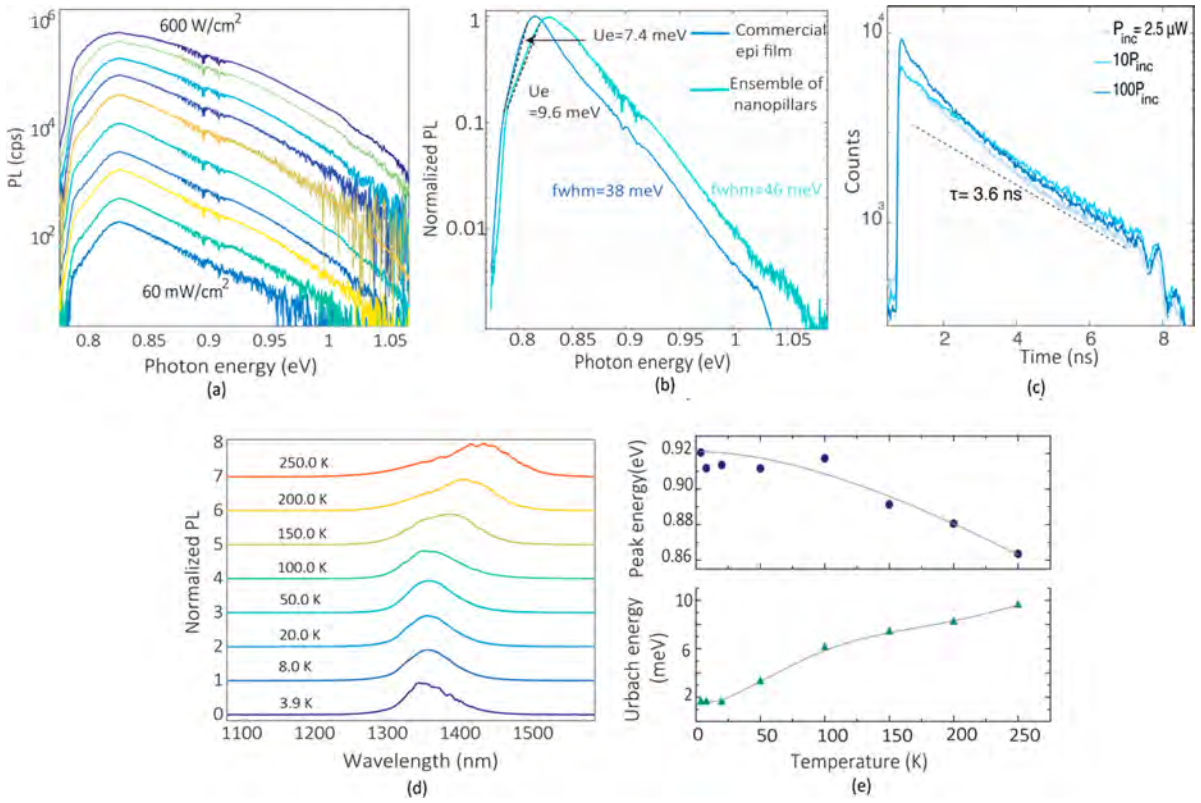

Figure 3. (a) Room-temperature, pump-dependent PL from five MWQ nanopillar heterostructure; (b) Comparison of emission from nanopillar MQWs with commercial epitaxial sample containing six pairs of InGaAs quantum wells; (c) Time-resolved PL measurement reveals a room-temperature lifetime of 3.6 ns at excitation powers of 2.5−250 μW; (d) Temperature-dependent PL spectra measured from a single nanopillar from 4 to 250 K; (e) Red-shift of the MQW spectrum follows the Varshni model $\left(E = E_0 - \frac{\alpha + T^2}{B + T}\right)$ using fitting parameter values (α = 5.45 × 10^{-4} eV/K, β = 337.78 K). Additionally, the Urbach energy decreases with temperature and reaches a limiting value of 1.6 meV below 20 K.

OPTICAL CHARACTERIZATION AND ROOM TEMPERATURE LASING

Excellent optical quality of the site-controlled InP is confirmed by photoluminescence measurements on as-grown nanopillars. Figure 2a shows room temperature PL spectra measured from a single nanopillar grown at 460 °C, for increasing excitation intensities of a continuous wave (cw) 660 nm pump. The strong peak at 1.42 eV corresponds to wurtzite InP and remains invariant with excitation. Also, no secondary peaks related to defects or polytypism were observed in the excitation dependent spectra. The emission line widths from site-controlled nanopillars were typically ∼50 meV, which is comparable to emission observed from spontaneously grown pillars, as shown in Figure 2b. We conclude that the presence of the silicon dioxide growth mask does not lead to formation of defects or polytypism in the nanopillar, and the material quality is equivalent to previously demonstrated, state-of-the-art InP nanopillars. Time-resolved photoluminescence (TRPL) was measured using femtosecond pulsed laser excitation at 680 nm and the data is analyzed using a monoexponential model (Figure 2c). The TRPL measurement was used to probe the carrier decay rate by incorporating an avalanche photodiode (APD) into the μ-PL setup. The measurement reveals room temperature lifetime in the range of ∼1.5−3.7 ns. As shown in the inset of Figure 2c, the lifetime increases with incident excitation and reaches a maximum value of 3.7 ns, following with a decrease again due to enhanced nonradiative recombination rate associated with Auger recombinations. The lifetime values are comparable to those measured in spontaneously nucleated InP nanopillars, which have previously showed a record long lifetime in the range of 2−7 ns.[33] Such a long room-temperature lifetime points toward excellent optical properties, low defect density, and a low, bulk-like surface recombination velocity. We estimate the surface recombination velocity to be of the order ∼1 × 10^3 cm/sec. Each as-grown nanopillar behaves as an optical cavity and supports helically propagating resonances. The modes are well-confined inside the cavity due to its large size, which allows large gain-mode overlap. As a result, we observe lasing in as-grown single nanopillars. Figure 2d demonstrates the spectra obtained when a single nanopillar is pumped optically by titanium-sapphire femtosecond laser (with 140 fs pulse width and 80 MHz repetition rate) at 730 nm. The lasing spectra were dispersed and then measured on a silicon CCD array. Below threshold, broad spontaneous emission is observed. A strong lasing peak at 873.5 nm dominates emission above threshold, with a sideband suppression ratio of ∼14 dB. A lasing threshold is observed at ∼1.6 mJ/cm^2 at room temperature. The line width collapses to ∼1.5 nm and a Q-factor of the nanopillar cavity can be estimated to be $Q \approx \lambda/\Delta\lambda_{th}$ = 582.[40] More details on the lasing characteristics are presented in Supporting Information.

GROWTH AND CHARACTERIZATION OF NANOPILLAR MULTIQUANTUM WELLS

For a silicon photonics optical link, the emitter should operate in the silicon transparent regime, ideally in the 1310−1550 nm

DOI: 10.1021/acsphotonics.7b00065
ACS Photonics 2017, 4, 695−702

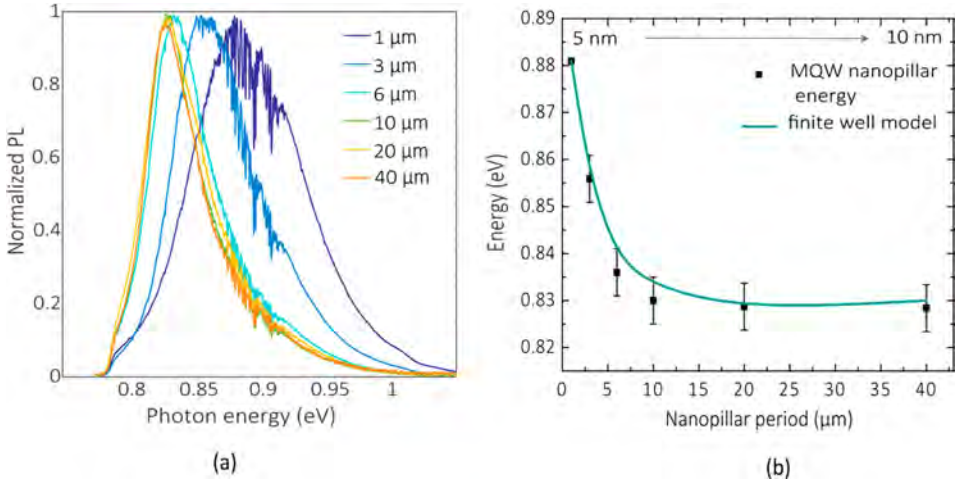

Figure 4. (a) Variation of MQW emission from pillars in different arrays (1−40 μm) on the same chip due to change in local TMIn flux. (b) Red-shift of quantum well emission with increasing array periods can be attributed to increase in quantum well thickness. Continuous line models the energy using a finite well model for QWs with varying thicknesses.

range. We achieved this by incorporating core−shell InGaAs/InP quantum wells in the site-controlled nanopillars. Quantum well growth is achieved by switching MOCVD precursors from TMIn and TBP to TMIn, TeGa, and TBAs, while maintaining group V overpressure throughout. The growth of the multiquantum (MQW) well stack is carried out at 455 °C in the same growth mode as the n-InP core. The high optical quality of MQW growth is confirmed through nonresonant μ-PL measurements on a single nanopillar. Pump-dependent PL measurement from a single nanopillar with five MQW shows emission in the silicon transparent wavelength regime (Figure 3a). No shift in emission wavelength or emergence of secondary peaks was observed with increase in pumping. Its superior optical quality is attested by internal quantum efficiency of ∼30% measured from temperature dependent photoluminescence measurements (Supporting Information). The quantum wells in a single nanopillar were directly excited using a continuous wave pump at 980 nm, focused to a spot less than 5 μm in diameter using a 100× objective. After filtering the pump wavelength, the quantum well photoluminescence was dispersed using a Princeton Instruments SP2750 spectrometer, and collected on a LN2 cooled OMA-V InGaAs array. We compared the MQW emission characteristics with a commercial epitaxy wafer consisting of six pairs of InGaAs quantum wells (Figure 3b). The nanopillar MQW sample shows a narrow room-temperature line width of ∼46 meV, which is comparable to 38 meV measured in the epitaxial wafer, suggesting quantum well uniformity and minimal inhomogeneous broadening. The spectra over the 0.78−0.82 eV regimes give the Urbach tail. An exponential tailing of the sub-bandgap states in the PL spectra gives a measure of material disorder and thus the Urbach energy. The Urbach tail is generally broad in nanowires and nanostructures due to crystallographic defects and surface states. Surprisingly, the Urbach energy in the MQW nanopillars is 10 meV when compared to 7.4 meV measured in the commercial epitaxial wafer. Previous reports of Urbach energy in InP-based nanowires are significantly higher (wurtzite ∼ 33 meV and zinc blende ∼ 24 meV).[41] Lifetime of the InGaAs MQW emission was measured at room temperature under incident powers varying from 2.5 to 250 μW using a 1000 nm pump. The temporal decay was detected using an InGaAs CCD and reveals an exponential decay rate of 3.6 ns (Figure 3c). The long lifetime and its invariance with pump power is attributed to the excellent material quality and carrier confinement in the MQW. Temperature-dependent PL spectra from nanopillar MQWs are presented in Figure 3d. For temperature-controlled measurements, the nanopillar sample was placed in a continuous-flow liquid helium cooled cryostat, with closed loop temperature control between 5 and 300 K. A strong dominant InGaAs quantum well peak is observed up to 4 K. The peak energy of the InGaAs MQW shows a red shift with increasing temperature due to bandgap shrinkage. The peak energy as a function of temperature follows the trend predicted by the Varshni relation, as shown in Figure 3e. The data measured from the nanopillar MQW agrees with the Varshni relation with fitting parameters $\alpha = 5.45 \times 10^{-4}$ eV/K and $\beta = 337.78$ K, which are typical for InGaAs.[20] The Urbach energy was also extracted from the temperature-dependent spectra. As seen in Figure 3e, the Urbach energy reduces with decrease in temperature and reaches its minimum value of 1.6 meV around 20 K. This corresponds to the disorder originating from the inhomogeneous broadening inherent in InGaAs quantum wells.

Silicon transparent emission in the range from 1400 to 1500 nm is observed for different growth periods on the same chip. The MQW emission red-shifts from 1405 to 1512 nm, with increasing growth pitch. This effect may be due to two concurrent factors: (a) Increased In incorporation on ⟨110⟩ plane quantum wells in larger pitch arrays due to reduced competition for TMIn adatoms during MQW growth. (b) Increase in InGaAs quantum well thickness due higher growth rate resulting from larger local TMIn flux. Transmission electron microscopy studies on similarly grown InGaAs quantum wells in spontaneously nucleated InP pillars show a radial InGaAs thickness of 5 nm.[42] These spontaneous nanopillars are identical to pillars in 1 μm arrays in dimension, where we may assume a quantum well thickness of 5 nm. Both InP and InGaAs growth rates increase, as local group III (TMIn) flux increases with pitch. The InGaAs quantum well thickness in subsequent higher pitch arrays can be assumed to scale up with the diameter of nanopillar. The measured PL energy is plotted in Figure 4 along with modeled energies derived from a finite quantum well taking into account

DOI: 10.1021/acsphotonics.7b00065
ACS Photonics 2017, 4, 695−702

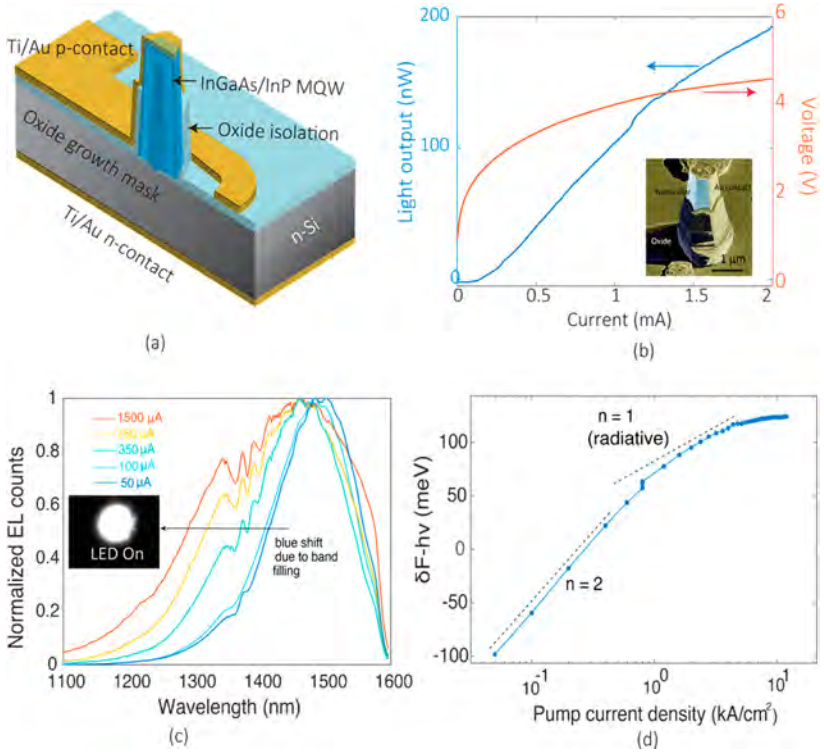

Figure 5. (a) Schematic of fabricated nanopillar MQW LED device. (b) L-I-V characteristics of a multipillar LED at room temperature. Inset shows an SEM image of one such nanopillars with an angle-evaporated Ti/Au contact. (c) Electroluminescence spectra from a single nanopillar measured for increasing injection currents. Inset shows a CCD image of a single nanopillar LED. (d) Fermi level split calculated from calibrated EL measurement for varying injection current densities shows a radiative dominant ideality factor of $n = 1$ at higher injection currents, as well as Fermi level splitting δF in the active region exceeding the bandgap.

quantum well thickness variation. The experimentally measured MQW emission is in good agreement with the modeled data.

ELECTROLUMINESCENCE FROM NANOPILLAR LED

To realize an electrically driven nano-LED, five InGaAs quantum wells were incorporated in the active region of a p-n diode. The grown structure consists of n-InP/InGaAs MQW/p-InP/p-InGaAs, grown in core−shell mode on n^+-Si, as shown schematically in Figure 5a, using DeTe and DeZn as n- and p-dopants, respectively. Because each single pillar is grown at a predetermined position on the chip, it can be processed via an optical lithography process and used as a single nano-LED device. Because the nanopillars grow in core−shell form, the n-doped core of the nanopillar is in contact with n-Si, which the p-doped shell grows over the oxide mask, eliminating the shunt path from the p-doped shell and n-Si substrate. For additional electrical isolation an oxide shoulder is fabricated. 20/200 nm of Ti/Au is evaporated via angled electron beam evaporation onto a highly p-doped InGaAs contact layer. The bare nanopillar region without metal is used to collect electroluminescence from the LED.

As shown in Supporting Information, room-temperature current−voltage characteristics from a single pillar show diode behavior with a series resistance of ∼40 KΩ, which is limited by the device dimensions. At low pump currents (below 100 μA) the injected carriers recombine nonradiatively, leading to a quadratic dependence of light output on current as shown in Supporting Information. Figure 5b shows the L-I-V characteristics of a nanopillar LED. The light output was measured using a Ge detector and a 100× objective lens. Details on the measurement setup can be found in Supporting Information. The LED exhibits bright emission with output power ∼200 nW. The collection efficiency of the setup is estimated to be ∼5%, which leads to an actual light output ∼4 μW, which is the highest reported light output from a nanopillar/nanostructure-based LED.[10,43,44] The inset of Figure 5b shows a high magnification SEM image of a single nanopillar after fabrication. Figure. 5c shows room-temperature electroluminescence spectra from a single nanopillar at ∼1510 nm with increasing injection. The inset of Figure 5c shows the emission of a nanopillar LED imaged on an InGaAs CCD.

Room-temperature EL shows strong quantum well emission, with no signal from the InP cladding. A calibrated electroluminescence measurement was used to determine the quasi Fermi level splitting of the carriers injected into the quantum well. The Fermi level split is directly related to the externally emitted EL counts from the nanopillars,[45] Under sufficiently high pump, intense electroluminescence counts lead to a calculated Fermi level split δF exceeding the EL peak energy $h\nu$, indicating that the device has been electrically biased beyond the transparency condition and into optical gain (see Figure 5d). The EL spectrum blue shifts due to the filling of the QW states, further corroborating the conclusion that the device has been biased beyond transparency. Heating-induced red shift was observed in the spectra only at the highest injection currents (∼10 kA/cm^2), attesting to the thermal robustness of the device.

DISCUSSION

In conclusion, we have investigated the site-controlled MOCVD growth of InP nanopillar heterostructures, directly on silicon (111), under CMOS-compatible conditions. The

DOI: 10.1021/acsphotonics.7b00065
ACS Photonics 2017, 4, 695−702

catalyst-free, low temperature nanopillar growth results in high yield of nanopillars. Their excellent optical performance is demonstrated by long lifetime (3.7 ns), low surface recombination velocity, and room-temperature lasing. Silicon transparent emission in the range of 1400−1500 nm is observed by incorporating InGaAs/InP quantum wells. The nanopillar quantum wells show remarkable optical properties, comparable to commercial epitaxial wafers and are introduced in the active region of a p-i-n nanopillar heterostructure. The device shows excellent diode behavior and bright electroluminescence ∼1500 nm, with an output power of 4 μW. Additionally, nanopillar diode devices also demonstrate strong photoresponse under reverse injection. This device is a first step toward the large-scale integration of highly efficient, ultracompact, bright light sources and, in general, nanophotonic devices for the silicon photonics toolbox.

■ ASSOCIATED CONTENT

Supporting Information

The Supporting Information is available free of charge on the ACS Publications website at DOI: 10.1021/acsphotonics.7b00065.

Additional optical and device characterization data with measurement techniques (PDF).

■ AUTHOR INFORMATION

Corresponding Author

*E-mail: cch@berkeley.edu.

ORCID

Saniya Deshpande: 0000-0002-7760-6604

Gilliard Malheiros-Silveira: 0000-0002-5176-3812

Connie Chang-Hasnain: 0000-0002-5341-6267

Author Contributions

†These authors contributed equally to this work.

Author Contributions

C.C.H. guided the overall project. S.D. developed the site-controlled nanopillar growth and performed MOCVD growth of nanopillars, MQW, and LED samples. S.D. performed SEM characterization. B.N.G. performed TEM characterization and FIB preparation of nanopillars for TEM. I.B., G.S., and W.M. performed optical characterization. I.B. fabricated LED devices and performed EL measurements. I.B. and S.D. analyzed the data. F.S. and K.C. assisted with MOCVD growth. S.D. prepared the manuscript.

Notes

The authors declare no competing financial interest.

■ ACKNOWLEDGMENTS

This work was supported by NSF Awards 1335609 and ECCS-0939514. Device fabrication was done in the Marvel Nanofabrication Lab at the University of California, Berkeley. We thank Dr. Emil Kolev in MOCVD repairs and maintenance. We thank Seth Fortuna for help with InGaAs QW TRPL characterization.

■ REFERENCES

(1) ITRS Report, http://public.itrs.net/reports.html, 2015.

(2) Miller, D. A. B. Rationale and challenges for optical interconnects to electronic chips. *Proc. IEEE* **2000**, *88*, 728−749.

(3) Heck, M. J. R.; Bowers, J. E. Energy efficient and energy proportional optical interconnects for multi-core processors: driving the need for on-chip sources. *IEEE J. Sel. Top. Quantum Electron.* **2014**, *20*, 1−12.

(4) Miller, D. Device requirements for optical interconnects to silicon chips. *Proc. IEEE* **2009**, *97* (7), 1166−1185.

(5) Schnitzer, I.; Yablonovitch, E.; Caneau, C.; Gmitter, T. J. Ultrahigh spontaneous emission quantum efficiency, 99.7% internally and 72% externally, from AlGaAs/GaAs/AlGaAs double heterostructures. *Appl. Phys. Lett.* **1993**, *62*, 131−133.

(6) Fang, A. W.; Park, H.; Cohen, O.; Jones, R.; Paniccia, M. J.; Bowers, J. E. Electrically pumped hybrid AlGaInAs-silicon evanescent laser. *Opt. Express* **2006**, *14*, 9203−9210.

(7) Duan, G.-H.; et al. Hybrid III−V on silicon lasers for photonic integrated circuits on silicon. *Proc. SPIE* **2014**, *20*, 158−170.

(8) Mi, Z.; Yang, J.; Bhattacharya, P.; Qin, G.; Ma, Z. High-performance quantum dot lasers and integrated optoelectronics on Si. *Proc. IEEE* **2009**, *97*, 1239−1249.

(9) Lee, A.; Jiang, Q.; Tang, M.; Seeds, A.; Liu, H. Continuous-wave InAs/GaAs quantum-dot laser diodes monolithically grown on Si substrate with low threshold current densities. *Opt. Express* **2012**, *20*, 22181−22187.

(10) Eggleston, M. S.; Messer, K.; Zhang, L.; Yablonovitch, E.; Wu, M. C. Optical antenna enhanced spontaneous emission. *Proc. Natl. Acad. Sci. U. S. A.* **2015**, *112*, 1704−1709.

(11) Egawa, T.; Hasegawa, Y.; Jimbo, T.; Umeno, M. Effects of dislocation and stress on characteristics of GaAs-based laser grown on Si by metalorganic chemical vapor deposition. *Jpn. J. Appl. Phys.* **1992**, *31*, 791−797.

(12) Groenert, M. E.; Leitz, C. W.; Pitera, A. J.; Yang, V.; Lee, H.; Ram, R.; Fitzerald, E. A. Monolithic integration of room-temperature cw GaAs/AlGaAs lasers on Si substrates via relaxed graded GeSi buffer layers. *J. Appl. Phys.* **2003**, *93*, 362−367.

(13) Larsson, M. W.; Wagner, J. B.; Wallin, M.; Håkansson, P.; Fröberg, L. E.; Samuelson, L.; Wallenberg, L. R. Strain mapping in free-standing heterostructured wurtzite InAs/InP nanowires. *Nanotechnology* **2007**, *18*, 015504.

(14) Dick, K. A.; Bolinsson, J.; Borg, B. M.; Johansson, J. Controlling the Abruptness of Axial Heterojunctions in III-V Nanowires: Beyond the Reservoir Effect. *Nano Lett.* **2012**, *12*, 3200−3206.

(15) Hersee, S. D.; Rishinaramangalam, A. K.; Fairchild, M. N.; Zhang, L.; Varangis, P. Threading defect elimination in GaN nanowires. *J. Mater. Res.* **2011**, *26*, 2293.

(16) Martensson, T.; Svensson, C. P. T.; Wacaser, B. A.; Larsson, M. W.; Seifert, W.; Deppert, K.; Gustafsson, A.; Wallenberg, L. R.; Samuelson, L. Epitaxial III-V NWs on silicon. *Nano Lett.* **2004**, *4*, 1987.

(17) Tomioka, K.; Yoshimura, M.; Fukui, T. A III-V nanowire channel on silicon for high-performance vertical transistors. *Nature* **2012**, *488*, 189−192.

(18) Ren, F.; Ng, K.; Li, K.; Sun, H.; Chang-Hasnain, C. J. High-quality InP nanoneedles grown on silicon. *Appl. Phys. Lett.* **2013**, *102*, 012115.

(19) Li, K.; Sun, H.; Ren, F.; Ng, K. W.; Tran, T. T. D.; Chen, R.; Chang-Hasnain, C. J. Tailoring the optical characteristics of microsized InP nanoneedles directly grown on silicon. *Nano Lett.* **2014**, *14*, 183−190.

(20) Chen, R.; et al. Nanolasers grown on silicon. *Nat. Photonics* **2011**, *5*, 170−175.

(21) Chuang, L. C.; et al. Critical diameter for III-V nanowires grown on lattice- mismatched substrates. *Appl. Phys. Lett.* **2007**, *90*, 043115.

(22) Ng, K. W.; Tran, T. D.; Ko, W. S.; Chen, R.; Lu, F.; Chang-Hasnain, C. Single Crystalline InGaAs Nanopillar Grown on Polysilicon with Dimensions beyond the Substrate Grain Size Limit. *Nano Lett.* **2013**, *13*, 5931−5937.

(23) Ng, K. W.; et al. Unconventional growth mechanism for monolithic integration of III−V on silicon. *ACS Nano* **2013**, *7*, 100−107.

(24) Lu, F.; Tran, T-T. D.; Ko, W. S.; Ng, K. W.; Chen, R.; Chang-Hasnain, C. J. Nanolasers grown on silicon-based MOSFETs. *Opt. Express* **2012**, *20* (11), 12171−12176.

DOI: 10.1021/acsphotonics.7b00065
ACS Photonics 2017, 4, 695−702

(25) Chen, R.; Ng, K. W.; Ko, W. S.; Parekh, D.; Lu, F.; Tran, T. D.; Li, K.; Chang-Hasnain, C. J. Nanophotonic integrated circuits from nanoresonators grown on silicon. *Nat. Commun.* **2014**, *5*, 4325−5325.
(26) Tomioka, K.; Motohisa, J.; Hara, S.; Hiruma, K.; Fukui, T. GaAs/AlGaAs core multishell nanowire-based light-emitting diodes on Si. *Nano Lett.* **2010**, *10*, 1639−1644.
(27) Holm, J. V.; Jørgensen, H. I.; Krogstrup, P.; Nygård, J.; Liu, H.; Aagesen, M. Surface-passivated GaAsP single-nanowire solar cells exceeding 10% efficiency grown on silicon. *Nat. Commun.* **2013**, *4*, 1498.
(28) Deshpande, S.; Heo, J.; Das, A.; Bhattacharya, P. Electrically driven polarized single-photon emission from an InGaN quantum dot in a GaN nanowire. *Nat. Commun.* **2013**, *4*, 1675.
(29) Duan, X.; Huang, Y.; Agarwal, R.; Lieber, C. M. Single-nanowire electrically driven lasers. *Nature* **2003**, *421*, 241−245.
(30) Yan, R.; Gargas, D.; Yang, P. *Nat. Photonics* **2009**, *3*, 569−576.
(31) Roest, A. L.; Verheijen, M. A.; Wunnicke, O.; Serafin, S.; Wondergem, H.; Bakkers, E. Position-controlled epitaxial III−V nanowires on silicon. *Nanotechnology* **2006**, *17*, 271−275.
(32) Fonseka, H.; Tan, H.; Wong Leung, Y.; Kang, J. H.; Parkinson, P.; Jagadish, C. High vertical yield InP nanowire growth on Si (111) using a thin buffer layer. *Nanotechnology* **2013**, *24* (46), 9.
(33) Li, K.; Ng, K. W.; Tran, T.-T. D.; Sun, H.; Lu, F.; Chang-Hasnain, C. J. Wurtzite-Phased InP Micropillars Grown on Silicon with Low Surface Recombination Velocity. *Nano Lett.* **2015**, *15*, 7189−7198.
(34) Ko, W. S.; Bhattacharya, I.; Tran, T. T. D.; Ng, K. W.; Gerke, S. A.; Chang, H. Ultrahigh Responsivity-Bandwidth Product in a Compact InP Nanopillar Phototransistor Directly Grown on Silicon. *Sci. Rep.* **2016**, *6*, 33368.
(35) Ko, W. S.; Tran, T. D.; Bhattacharya, I.; Ng, K. W.; Sun, H.; Chang-Hasnain, C. Illumination angle insensitive single indium phosphide tapered nanopillar solar cell. *Nano Lett.* **2015**, *15*, 4961.
(36) Mohan, P.; Motohisa, J.; Fukui, T. Controlled growth of highly uniform, axial/radial direction-defined, individually addressable InP nanowire arrays. *Nanotechnology* **2005**, *16*, 2903−2907.
(37) Gao, Q.; Saxena, D.; Wang, F.; Fu, L.; Mokkapati, S.; Guo, Y.; Li, L.; Wong-Leung, J.; Caroff, P.; Tan, H. H.; Jagadish, C. Selective-Area Epitaxy of Pure Wurtzite InP Nanowires: High Quantum Efficiency and Room-Temperature Lasing. *Nano Lett.* **2014**, *14*, 5206−5211.
(38) Watanabe, Y.; Hibino, H.; Bhunia, S.; Tateno, K.; Sekiguchi, T. Site-controlled InP nanowires grown on patterned Si substrates. *Phys. E* **2004**, *24*, 133−137.
(39) Tran, T.-T. D.; Chen, R.; Ng, K. W.; Ko, W. S.; Lu, F.; Chang-Hasnain, C. J. Three-dimensional whispering gallery modes in InGaAs nanoneedle lasers on silicon. *Appl. Phys. Lett.* **2014**, *105*, 111105.
(40) Hua, B.; Motohisa, J.; Ding, Y.; Hara, S.; Fukui, T. Characterization of Fabry-Pérot microcavity modes in GaAs nanowires fabricated by selective- area metal organic vapor phase epitaxy. *Appl. Phys. Lett.* **2007**, *91*, 131112.
(41) Maharjan, A.; Pemasiri, K.; Kumar, P.; Wade, A.; Smith, L. M.; Jackson, H. E.; Yarrison-Rice, J. M.; Kogan, A.; Paiman, S.; Gao, Q.; Tan, H. H.; Jagadish, C. Room temperature photocurrent spectroscopy of single zincblende and wurtzite InP nanowires. *Appl. Phys. Lett.* **2009**, *94*, 193115.
(42) Lu, F.; Li, K.; Ng, K. W.; Ko, W. S.; Chang-Hasnain, C. J. Characteristics of InP nanoneedles grown on silicon by low-temperature MOCVD. International Symposium on Compound Semiconductors (ISCS) and International Conference on Indium Phosphide and Related Materials (IPRM), 2015, Mo-1A.5.
(43) Sarwar, A. T. M.; May, B. J.; Deitz, J. I.; Grassman, T. J.; McComb, D. W.; Myers, R. C. Tunnel junction enhanced nanowire ultraviolet light emitting diodes. *Appl. Phys. Lett.* **2015**, *107*, 101103.
(44) Minot, E. D.; Kelkensberg, F.; Van Kouwen, M.; Van Dam, J. A.; Kouwenhoven, L. P.; Zwiller, V.; Borgström, M. T.; Wunnicke, O.; Verheijen, M. A.; Bakkers, E. P. A. M. Single quantum dot nanowire LEDs. *Nano Lett.* **2007**, *7*, 367−371.
(45) Tran, T-T D.; Sun, H.; Ng, K. W.; Ren, F.; Li, K.; Lu, F.; Yablonovitch, E.; Chang-Hasnain, C. J. High brightness InP micropillars grown on silicon with Fermi level splitting larger than 1 eV. *Nano Lett.* **2014**, *14*, 3235−3240.

DOI: 10.1021/acsphotonics.7b00065
ACS Photonics 2017, 4, 695−702